Global calcite cycling constrained by sediment preservation controls

John P. Dunne,[1] Burke Hales,[2] and J. R. Toggweiler[1]

Received 5 August 2010; revised 29 June 2012; accepted 17 July 2012; published 12 September 2012.

[1] We assess the global balance of calcite export through the water column and burial in sediments as it varies regionally. We first drive a comprehensive 1-D model for sediment calcite preservation with globally gridded field observations and satellite-based syntheses. We then reformulate this model into a simpler five-parameter box model, and combine it with algorithms for surface calcite export and water column dissolution for a single expression for the vertical calcite balance. The resulting metamodel is optimized to fit the observed distributions of calcite burial flux. We quantify the degree to which calcite export, saturation state, organic carbon respiration, and lithogenic sedimentation modulate the burial of calcite. We find that 46% of burial and 88% of dissolution occurs in sediments overlain by undersaturated bottom water with sediment calcite burial strongly modulated by surface export. Relative to organic carbon export, we find surface calcite export skewed geographically toward relatively warm, oligotrophic areas dominated by small, prokaryotic phytoplankton. We assess century-scale projected impacts of warming and acidification on calcite export, finding high sensitive to inferred saturation state controls. With respect to long-term glacial cycling, our analysis supports the hypothesis that strong glacial abyssal stratification drives the lysocline toward much closer correspondence with the saturation horizon. Our analysis suggests that, over the transition from interglacial to glacial ocean, a resulting $\sim$0.029 PgC a^{-1} decrease in deep Atlantic, Indian and Southern Ocean calcite burial leads to slow increase in ocean alkalinity until Pacific mid-depth calcite burial increases to compensate.

Citation: Dunne, J. P., B. Hales, and J. R. Toggweiler (2012), Global calcite cycling constrained by sediment preservation controls, *Global Biogeochem. Cycles*, *26*, GB3023, doi:10.1029/2010GB003935.

1. Introduction

[2] As the dominant form of $CaCO_3$ in marine sediments, the global ocean calcite budget has been a topic of great scientific interest for decades [*Li et al.*, 1969; *Broecker*, 1971; *Morse and Mackenzie*, 1990; *Milliman*, 1993; *Berelson et al.*, 2007]. An understanding of calcite cycling in marine sediments has recently become increasingly urgent to quantify the ocean sediment response to climate change and ocean acidification [*Feely et al.*, 2004; *Orr et al.*, 2005].

[3] The most globally extensive constraint on calcite cycling is the geographical pattern of calcite burial [e.g., *Catubig et al.*, 1998]. The accumulation of calcite on the seafloor follows a well-described pattern: Atlantic sediments typically have more calcite than Pacific sediments and sediments from below 5000 m typically have no calcite at all. This pattern is thought to exist for three reasons: 1) calcite is more soluble at greater depths; 2) planktonic organisms produce more calcite than is needed to balance the inputs of calcium and bicarbonate ions from rivers; and 3) the deep circulation pathways lead to more corrosive deep waters in the Pacific than in the Atlantic as the seafloor in the Atlantic is bathed in recently ventilated North Atlantic Deep Water (NADW), which is low in CO_2 and relatively high in CO_3^{2-}. Water in the unventilated deep Pacific, on the other hand, are high in CO_2 and low in CO_3^{2-}, attributes that favor dissolution rather than preservation.

[4] The concept of the lysocline has proved a convenient means of describing this dynamic. If thermodynamic solubility equilibrium with bottom water is assumed, the lysocline's position is determined via a simple formula by the input of calcium to the ocean from rivers and the hypsometry of the seafloor. To this end, *Li et al.* [1969] cited *Livingstone* [1963] and *Turekian* [1964] to the effect that 1×10^{13} moles of calcium ions come into the ocean via rivers every year. At a steady state, and ignoring other forms of $CaCO_3$, the same number of moles of calcite must be buried on the seafloor. If one assumes that the rain of calcite to the seafloor is uniform, the fraction of the seafloor below the calcite

[1]NOAA Geophysical Fluid Dynamics Laboratory, Princeton, New Jersey, USA.
[2]College of Oceanic and Atmospheric Sciences, Oregon State University, Corvallis, Oregon, USA.

Corresponding author: J. P. Dunne, NOAA Geophysical Fluid Dynamics Laboratory, PO Box 308, Princeton, NJ 08542, USA. (john.dunne@noaa.gov)

0886-6236/12/2010GB003935

lysocline and mostly free of calcite should be quantitatively related to the global production of calcite and the extent to which the global production exceeds the river input.

[5] However, sediments with 80% $CaCO_3$ are found well below the saturation horizon in certain areas, e.g., below 4200 m in the equatorial Pacific [*Farrell and Prell*, 1989] and below 5000 m over most of the Atlantic [*Biscaye et al.*, 1976]. Indeed, in regions of the Atlantic and Pacific where surface calcite export is relatively high, the sediments in the two oceans are more alike than they are different in both having 20–40% $CaCO_3$ at 5000 m [*Biscaye et al.*, 1976; *Berger et al.*, 1976]. In these areas, thermodynamic equilibrium with bottom water solubility is overcome with high input of dissolving calcite allowing sediment pore waters to become buffered with respect to dissolution. Significant amounts of dissolution also take place at depths above the calcite lysocline as respiration of organic matter depresses the calcite saturation state in pore waters [*Emerson and Bender*, 1981; *Sayles*, 1985; *Archer*, 1996; *Hales et al.*, 1997; *Hales*, 2003]. In both cases, a rate dependent kinetic factor is overpowering the bottom water thermodynamic constraint: in one case, a high rate of calcite input is promoting preservation; in the other a high rate of organic matter input is promoting dissolution.

[6] In order to develop a self-consistent representation of the global ocean calcite cycle, this paper quantifies the three main components of the vertical calcite balance as it varies regionally through surface calcite export, water column dissolution, sediment dissolution, and burial. Using a combination of satellite-based export estimates and sediment-based burial estimates, we map calcite burial efficiency, defined as the rate of accumulation of calcite (or "burial flux") divided by the input of calcite to the sediments. We estimate burial efficiency via the 1-D sediment and pore water model of *Hales* [2003] and *Hales and Emerson* [1996, 1997b], and includes the kinetic additions of alkalinity and DIC via respiration and dissolution, and heterogeneous-medium diffusive transport of the major individual species that make up alkalinity and DIC. Briefly, the 1-D model incorporates along with, bottom water thermodynamic controls, two pore water kinetic factors: the ability of calcite dissolution within sediments to raise pore water saturation state, the respiration of organic matter to lower saturation state. This manuscript thus assumes multithousand year steady state equilibrium between weathering, calcite export based on satellite chlorophyll, ocean chemistry based on recent field programs, and calcite distributions in the sediment mixed layer.

[7] The *Hales* [2003] 1-D model is then reduced to a box model that can be combined with the surface export and water column attenuation to produce a metamodel for the vertical balance in a single equation. The metamodel is simple enough to be optimized in a formal stepwise way, which allows us to improve the algorithm that links the production of organic matter seen by satellites to the surface export of calcite. In the end, our optimized meta-model is able to explain about 60% of the spatial variance in the observed burial of calcite. The metamodel is then used to predict changes in the export and burial of calcite from preindustrial times to the end of the 21st century in response to changes in surface temperature and ocean chemistry, as well as to test current hypotheses coupling changes in calcite cycling and CO_3^{2-} distributions during glacial periods of the last 800 K years.

[8] The surface export optimized by our calcite metamodel is only that portion that directly relates to fluxes of calcite between the upper ocean and burial on the seafloor. Our model does not address the total $CaCO_3$ production as we ignore more easily dissolved forms that have been argued to be decoupled from sediment burial [*Milliman et al.*, 1999; *Feely et al.*, 2002; *Chung et al.*, 2003], though high upper water column dissolution has also been disputed [*Friis et al.*, 2006]. In either case, production of $CaCO_3$ from aragonite, high Mg-calcite and other more easily dissolved forms of $CaCO_3$ is largely invisible to our analysis given our emphasis on export fluxes to the deep ocean and sediment cycling.

2. Methods

2.1. Initial Burial Efficiency From Satellite and Sediment Observations

[9] Our initial algorithm for calcite export from the surface is derived from the global one-degree gridded data sets for primary production and particulate organic carbon export (F_{POC}) described in *Dunne et al.* [2007]. The sinking flux of calcite is assumed to be proportional to F_{POC}. Regionally varying $Ca{:}C_{org}$ utilization ratios, estimated by *Sarmiento et al.* [2002] from upper-ocean alkalinity and nitrate gradients, are used to scale the calcite flux. F_{POC} used in our initial algorithm is the product of the local primary production averaged from three satellite-based estimates and the local particle export ratio as a function of sea surface temperature and chlorophyll concentration.

[10] Dissolution of calcite in the water column is assumed to occur only where the water is undersaturated. This assumption is supported by our investigation of the global data compilation of *Honjo et al.* [2008] for which the only site for which we could find a strong and persistent gradient in $CaCO_3$ was for Station PAPA (50°N, 145°W). Based on the full set of time series observations in *Wong et al.* [1999] for Station PAPA in which 33% ± 2% (using 1983, 1985, 1989 and 1990, but excluding 1993 which suggested allochthonous import of $CaCO_3$ at depth) of the $CaCO_3$ flux in the 1000 m was dissolved by the 3800 m trap in a water column with an average saturation state of 0.81, we assume a dissolution length scale (z_{Diss}) proportional to the degree of undersaturation via:

$$F_{Bottom} = F_{Surface} \cdot \exp(-\Delta z_{Undersat} \cdot \max(0, 1 - \Omega_{UndersateAve})/z_{Diss}) \quad (1)$$

where $\Delta z_{Undersat}$ is the depth interval that is undersaturated with respect to calcite, and $\Omega_{UndersatAve}$ is the average saturation state in that depth interval. We derive an initial value for z_{Diss} based on *Wong et al.* [1999] of 1343 m.

[11] To calculate bottom water saturation state (Ω), data for temperature and salinity were taken from the World Ocean Atlas 2001 database [*Conkright et al.*, 2002]; while for dissolved inorganic carbon and alkalinity were taken from the Carbon Dioxide Information Analysis Center database [*Key et al.*, 2004]. Carbonate ion concentrations were calculated using OCMIP II biotic protocols [*Najjar and Orr*, 1998] (http://www.ipsl.jussieu.fr/OCMIP/phase2/

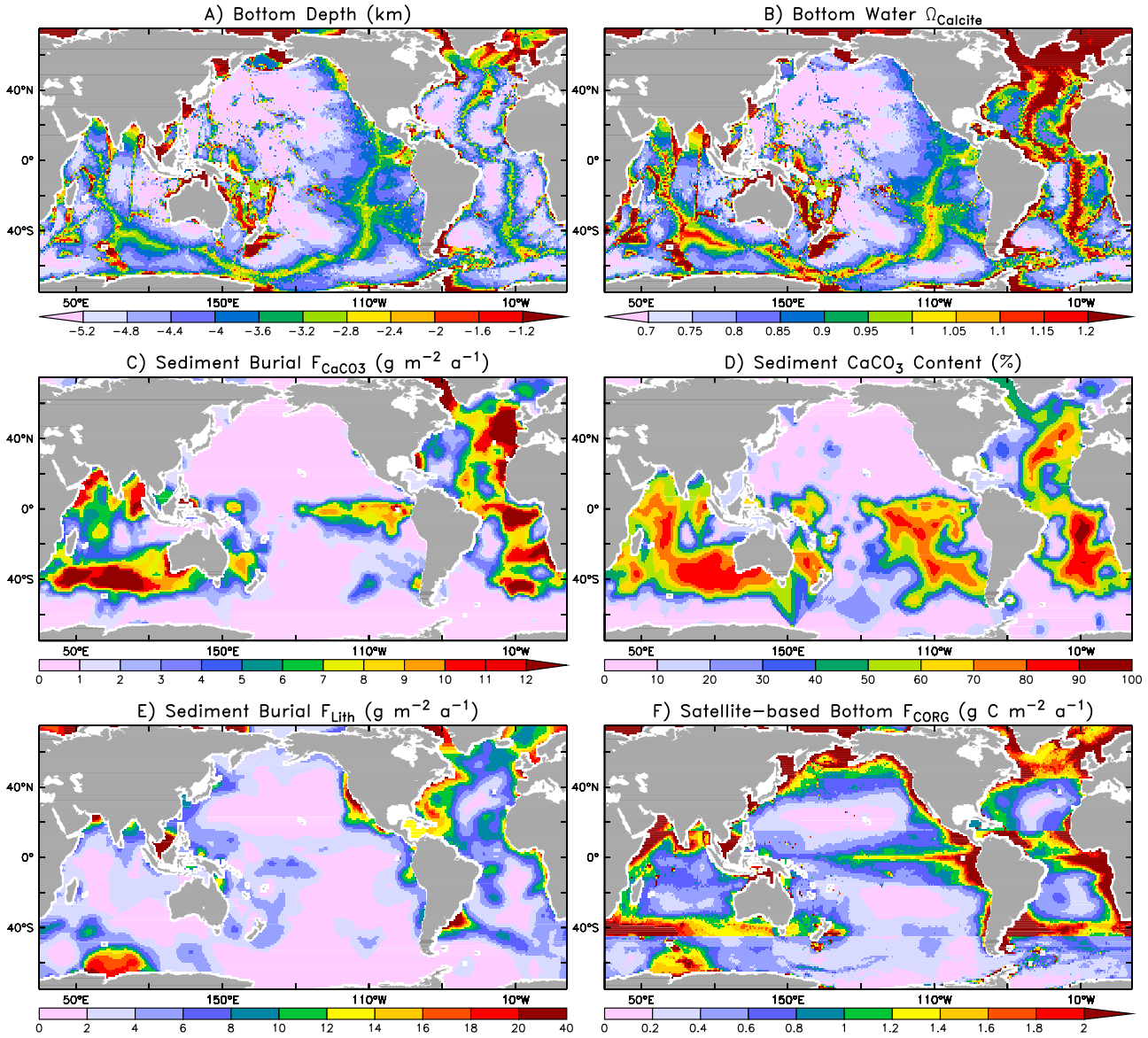

Figure 1. Global maps of observation-based bottom properties and fluxes. (a) Bottom depth (m). (b) Calcite saturation state of bottom water (Ω). (c) Burial flux of $CaCO_3$ based on sediment observations. (d) $CaCO_3$ content of modern sediment (%) based on sediment observations. (e) Burial flux of lithogenic material based on sediment observations. (f) Initial estimate for the flux of organic carbon to the ocean bottom derived from the satellite based synthesis of *Dunne et al.* [2007]. All maps are based on a $1^\circ \times 1^\circ$ grid. Accumulation rate synthesis for $CaCO_3$ and lithogenic material is from *Dunne et al.* [2007], based on the sediment composition work of *Seiter et al.* [2004] and accumulation rate information from *Jahnke* [1996], M. Zabel (personal communication, 2006) and D. Archer (personal communication, 2006).

simulations/Biotic/HOWTO-Biotic.html). The saturation state with respect to calcite was determined using the *United Nations Educational, Scientific and Cultural Organization* [1987] algorithm. See auxiliary material for the surface and bottom input values used in this study.[1]

[12] Maps of the bottom depth and the saturation state of bottom water (Ω) are shown in Figures 1a and 1b, respectively. To be consistent with the limitations of the sediment data sets, our analysis is restricted to water depths greater than 1000 m and latitudes between 67°S and 67°N. The decrease in Ω between the North Atlantic and North Pacific reflects the build-up of respired CO_2 along the path of the deep circulation while higher values of Ω are seen above relatively shallow areas of the seafloor. Our primary constraints come from sediment $CaCO_3$ content (Figure 1d) and burial fluxes of $CaCO_3$ (Figure 1c) and lithogenic material (Figure 1e) compiled from sediment observations [*Seiter et al.*, 2004; *Dunne et al.*, 2007]. Additionally, we show

[1]Auxiliary material data sets are available at ftp://ftp.agu.org/apend/gb/2010GB003935. Other auxiliary material files are in the HTML. doi:10.1029/2010GB003935.

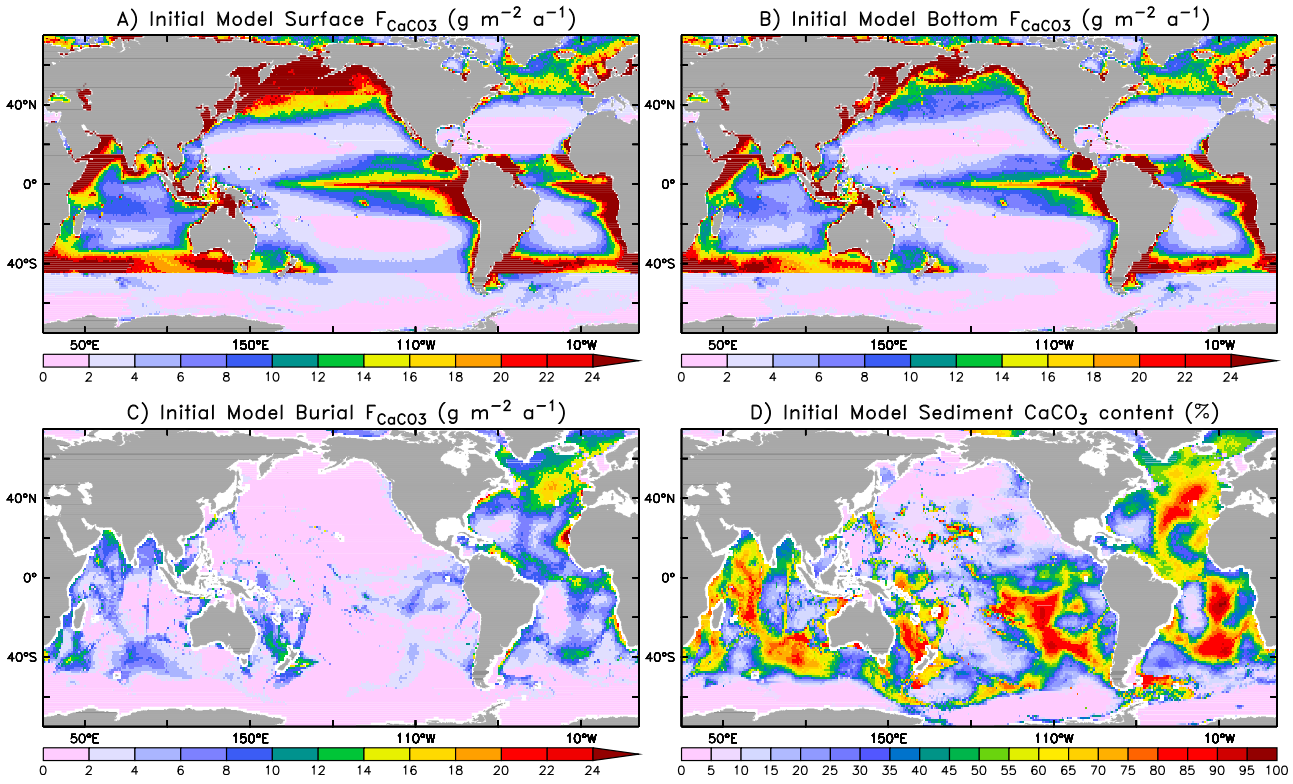

Figure 2. Initial satellite-based inputs for the calculation of sediment preservation efficiency from *Dunne et al.* [2007]. (a) Initial estimate for the sinking flux of $CaCO_3$ out of the surface. (b) Initial estimate for the flux of $CaCO_3$ to the bottom. (c) Initial estimate for the burial flux of $CaCO_3$. (d) Initial estimate for the $CaCO_3$ content of modern sediment (%).

our initial estimate for the organic matter flux to the bottom based on Dunne *et al.* [2007]. The $CaCO_3$ burial flux (Figure 1c) is highest in the eastern Atlantic, both north and south, in the southern Indian, and in the equatorial Pacific. In line with the shallower depths and higher values of Ω, the observations indicate more accumulation east of the mid-Atlantic Ridge than to the west. To a rough extent the burial flux tends to be high in the Atlantic where Ω is high, and very low in the North Pacific where Ω is low. The burial flux calculated for the equatorial Pacific appears to be high despite a low Ω. The $CaCO_3$ content of the sediments in Figure 1d overlaps fairly well with the burial flux except that $CaCO_3$ values in the south tend to be higher because there is less dilution by lithogenic material. The total open-ocean burial flux in our data set is 0.130 PgC a^{-1}, similar to the value given by *Milliman* [1993] and about 30% higher than the amount given by *Catubig et al.* [1998].

[13] Figure 2a shows our initial estimate for the satellite-derived surface calcite export (F_{Surf}). The sharp contrasts in flux at 15° and 45° North and South in Figure 2 are due to the associated contrast in the areal average $Ca:C_{Org}$ ratios from *Sarmiento et al.* [2002] which were taken as constant values across the 90°S–45°S, 45°S–15°S, 15°S–15°N, 15°N–45°N, and 45°N–90°N latitude bands for each ocean. Figure 2b shows our initial satellite-derived flux to the bottom, as determined by our initial algorithm for the surface export and our initial algorithm for water column dissolution. These results constitute our "control case" from (1). Our initial estimate for the flux to the bottom is highest in the equatorial upwelling zones, the subantarctic zones in the south, and north of 40°N in the North Pacific. These are areas where the satellite-based primary production is especially high. Our initial flux to the bottom is very low in the subtropical gyres where the satellite-based primary production is very low. The observed burial fluxes in Figure 1c suggest that there might be a strong skew in the flux to the bottom toward the Atlantic, but nothing of this sort is seen in our initial estimate. The upwelling zones off the Atlantic coast of Africa and off the Pacific coast of South America and the entire subpolar zone of the North Pacific also have much larger inputs to the bottom than one would surmise from the observed burial fluxes.

[14] In a first step to achieve a more mechanistic representation, the one-dimensional (1-D) sediment and pore water model of *Hales* [2003] is used to generate an initial map of synthetic burial fluxes in Figure 2c. These results take into account the saturation state of the overlying water in Figure 1b, the fluxes of calcite to the bottom in Figure 2b, and the fluxes of organic carbon and lithogenic material to the bottom in Figures 1f and 1e, respectively. Parameter values for the 1-D sediment model are taken from *Hales* [2003] for the Ceara Rise site except for the dissolution rate constant which was set to 0.004%/day (the average value for the Ceara Rise and Ontong Java Plateau sites). Organic respiration in the sediment is partitioned into fast and slow pathways as a function of organic carbon input based on Figure 2 of *Hales* [2003]. The initial sediment composition ($\%CaCO_3$) that we derive from the burial fluxes

in Figure 2c and the observed inputs of lithogenic material in Figure 1e is shown in Figure 2d. As one might expect from the bottom fluxes in our control case, our synthetic sediments in the subpolar North Pacific and in the upwelling zones along the African and South American margins are much more carbonate-rich than the actual sediments (Figure 1d).

2.2. Metamodel of Burial Efficiency

[15] In order to devise a simple description for the preservation in the sediment amenable to implementation in a global metamodel, the 1-D model of *Hales* [2003] is reduced here to a box model. The calcite mass of a sediment layer of constant thickness results from the steady state balance of three fluxes: the calcite flux into the box at the sediment-water interface (F_{Btm}; g m^{-2} a^{-1}), the dissolution in the box (F_{Diss}; g m^{-2} a^{-1}), and permanent burial flux out at the bottom (F_{Bur}; g m^{-2} a^{-1}), i.e.:

$$\Delta z \cdot \Delta C/\Delta t = F_{Btm} - F_{Diss} - F_{Bur} \quad (2)$$

where C is the concentration of calcite in the sediment box (g m^{-3}). While alternative approximations based on simple plug flow were also considered, the best approximation for C was found empirically by normalizing to the limiting case of a pure calcite sediment ($C_0 = 2.7 \times 10^6$ $(1 - 0.7) = 8.1 \times 10^5$ g m^{-3}; assuming a dry density of 2.7 g cm^{-3}, and constant porosity of 0.7) and equating the ratio of C to C_0 to the ratio of the burial flux (F_{Bur}) to the incoming flux to the sea bottom (F_{Btm}):

$$F_{Bur}/F_{Btm} = C/C_0 \quad (3)$$

In order to represent the dissolution term, we began with a simple representation of dissolution as a linear function of calcite undersaturation:

$$F_{Diss} = \Delta z \cdot \gamma \cdot (1 - \Omega_{Btm}) \cdot C, \Omega_{Btm} < 1; F_{Diss} = 0, \Omega_{Btm} \quad (4)$$

where Δz is the depth of the sediment layer, γ is the dissolution rate constant, and Ω_{Btm} is the bottom water calcite saturation state. The dissolution flux is assumed to be zero if the expression inside the parentheses is negative, i.e., if Ω_{Btm} is greater than 1. The box model, by definition, cannot resolve pore water differences within Δz so the saturation state of the pore water in the box model is initially assumed to be the same as in the overlying water.

[16] To this initial representation, we added terms to account for four additional factors controlling calcite preservation in the 1-D model of *Hales* [2003]. The four factors introduced in sequential optimizations are: 1) enhanced dissolution by fast respiration near the sediment surface, 2) enhanced dissolution by slow respiration in deeper pore waters, 3) an exponential term in the bulk dissolution rate constant to account for the vertical nonlinearity in pore water dissolution, and 4) an exponential term that enhances the burial of calcite when the total sediment accumulation is especially high. We account for the first three factors with the following form for F_{Diss}:

$$F_{Diss} = \phi_R \cdot F_{Org} + \Delta z \cdot \gamma \cdot \left(1 - \Omega_{Btm} + \phi_{Org} \cdot F_{Org}\right)^{\alpha} C \quad (5)$$

where ϕ_R is a dimensionless dissolution efficiency term for respiration of the organic flux (F_{Org}; g m^{-2} a^{-1}) driving dissolution near the sediment interface, ϕ_{Org} (g^{-1} m^2 a) is an efficiency term a lowering the pore water saturation state due to slow organic matter respiration within pore waters, and γ is the dissolution rate constant in a^{-1} set to zero if the overall saturation term in parentheses is greater than zero. The exponent α in (5) is included to enhance the linear dissolution rate when the saturation state of the overlying water is particularly low and avoid burying significant amounts of calcite under linear dissolution. This effect was captured by the *Hales* [2003] model representation, where the near-interfacial pore waters and the sensitivity of near interfacial dissolution to overlying bottom water saturation were well resolved. The simplicity of the current approach requires the empirical exponent to adequately reproduce the dissolution nonlinearity in the full model. In order to represent situations in which sediment rates decouple pore water saturation states from the overlying water, we allow the thickness of the sediment layer exposed to active dissolution (Δz; m) to vary. Thus, Δz in (5) is made a function of the incoming flux of lithogenic material (F_{Lith}; g m^{-2} a^{-1}) and calcite, $\Delta z = (F_{Lith} + F_{Btm}))^{\beta}$. The exponent β, in this case, is a negative number, which means that the thickness of the layer exposed to dissolution is small when the accumulation rate is large.

[17] Finally we arrive at an expression for the fractional preservation of calcite in the sediment layer ($f_{Meta} = F_{Bur}/F_{Btm}$) by inserting (5) into (2), solving (2) for C at steady state, and substituting into (3) to give:

$$f_{Meta} = \left(F_{Btm} - \phi_R \cdot F_{Org}\right)/\left(\gamma \cdot \left(1 - \Omega_{Btm} + \phi_{Org} \cdot F_{Org}\right)^{\alpha} \cdot (F_{Lith} + F_{Btm}))^{\beta} C_0 + F_{Btm}\right) \quad (6)$$

where the dissolution term, $\gamma \cdot (1 - \Omega_{Btm} + \phi_{Org} \cdot F_{Org})$, is set equal to zero if the value in the parentheses is negative, i.e., if the effective saturation state is greater than 1. f_{Meta} is restricted to vary between 0 and 1.

2.3. Optimization of Sediment Preservation Metamodel

[18] The metamodel is optimized in three sequential steps which were then iterated until convergence was reached. First, the 1-D model is run globally to get burial fluxes. Second, the box model is optimized to reproduce the meta-behavior of the 1-D model. Third, burial fluxes from the optimized box model are optimized against the observed burial fluxes through a suite of alternative algorithms for surface calcite export (F_{Surf}). On the second iteration step three, we were additionally able to solve for a revised value for z_{Diss}. In order to derive optimal parameter values for ϕ_R, ϕ_{Org}, γ, α, and β, we solved for candidate values of f_{Meta}. The Matlab™ multidimensional search algorithm *fminsearch* based on the Nelder-Mead, or downhill simplex, method [*Nelder and Mead*, 1965] was used, augmented to include bounds that restrict the search to scientifically viable parameter space. In order to generate a roughly normal error distribution, the cost function to be minimized was structured as the sum of the difference of square root preservation efficiencies between the 1-D model and metamodel over the globe from 67°S to 67°N for water depths greater than 1000 m. The results of the stepwise optimization are presented in Figure 3 and Table 1, starting with the linear dissolution rate, γ. Figure 3 compares the burial efficiency, f, derived from the box model for each 1-deg. square of

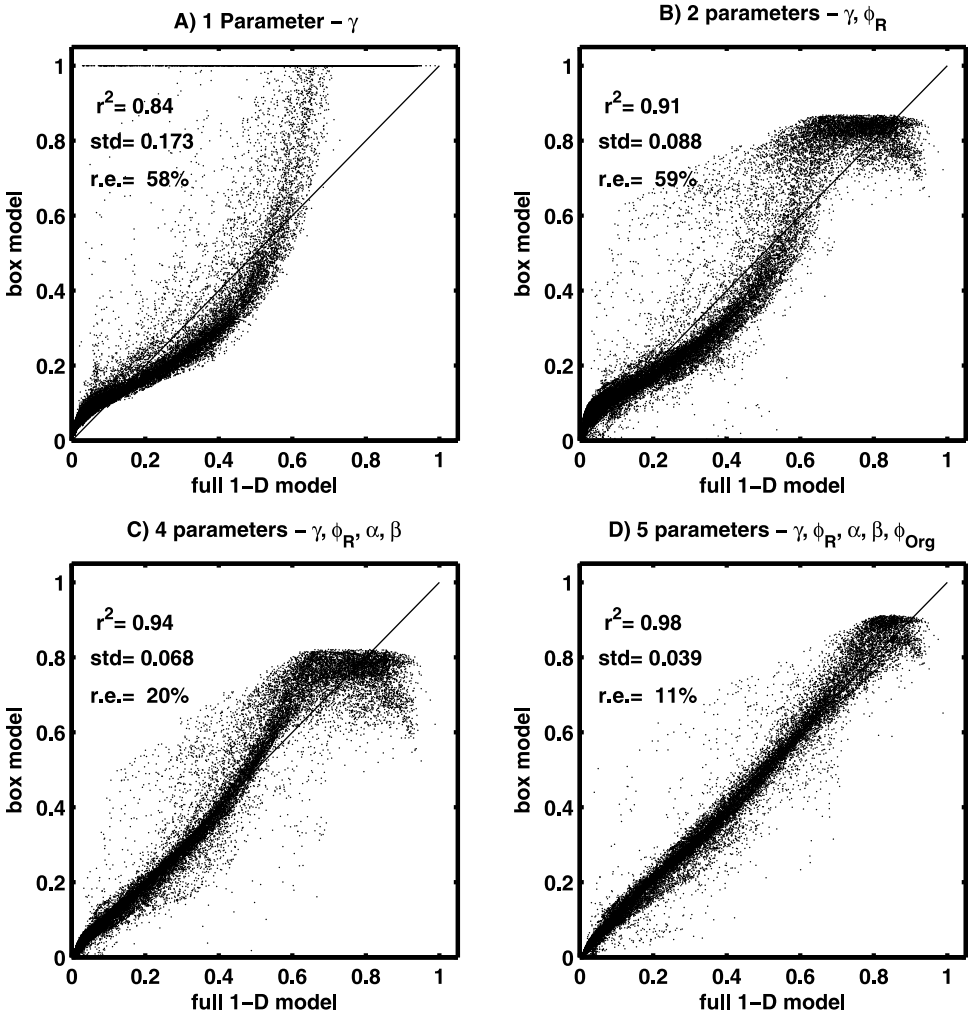

Figure 3. Scatterplot comparing the *Hales* [2003] 1-D model derived burial efficiencies to the optimized metamodel described in (6) with 1, 2, 4, and 5 parameters as described in Table 1.

seafloor with the burial efficiency derived from the 1-D model. With z_{Diss} held fixed, all terms except γ were found to converge on the first iteration. See auxiliary material for sensitivity studies on interior dissolution. Convergent values for all parameters including and γ (Table 1) and z_{Diss} (643 m; Table 2) were found on the second iteration.

[19] With the dissolution rate constant, γ, as the only active parameter (Figure 3a), i.e., with ϕ_R and $\phi_{Org} = 0$ and the exponents, α and β equal to 1 and 0, respectively, the box model approaches the thermodynamic limit. This version of the box model yields many locations where burial efficiency is equal to unity - which is never the case in the 1-D model - and always preserves appreciable calcite even where the 1-D model has a burial efficiency of zero.

[20] Adding the rapid organic matter respiration term, $\phi_R \cdot F_{Org}$, in Figure 3b reduces the box burial efficiency in areas where the bottom waters are near saturation and allows for a lower dissolution rate constant overall (Table 1). This brings the two models into agreement in showing that there are no locations where all of the calcite coming into the sediments is preserved.

[21] In Figure 3c, a fixed value for Δz in (5) is replaced by $(F_{lith} + F_{Btm})^{\beta}$ and the two exponents are allowed to vary. As seen in the transition from Figure 3b to Figure 3c, the $(F_{lith} + F_{Btm})^{\beta}$ term in (6) makes an important contribution to reducing the relative error in the box model. When lithogenic and calcite inputs are relatively high, calcite is rapidly sequestered away from bottom waters, and more calcite is preserved. This raises intermediate burial efficiencies in the box model. Allowing α to be greater than 1 reduces the burial efficiency when dissolution is favored.

Table 1. Optimal Parameter Values for the Dissolution Rate Constant (γ; a^{-1}), Surface Dissolution Efficiency (ϕ_R; Dimensionless), Undersaturation Nonlinear Exponent (α), Dissolution Length Scale Nonlinear Exponent (β; Dimensionless), and Pore Water Dissolution Efficiency (ϕ_{Org}; $mol^{-1}\ m^{-2}\ a$) in 2, 3, 4, and 5 Parameter Versions of the Metamodel

Parameter	γ	ϕ_R	α	β	ϕ_{Org}
1	1.887×10^{-4}	0	1	0	0
2	1.345×10^{-4}	0.2164	1	0	0
3	1.300×10^{-4}	0.2729	1.037	0	0
4	1.642×10^{-3}	0.2951	1.231	−1.042	0
5	0.03607	0.14307	2.7488	−2.2185	4.1228

Table 2. Optimal Parameter Values and Regression Coefficients in Surface Export Parameterization Sensitivity Analysis in (7)[a]

Calcite Export Algorithm	z_{Diss}	r_{FPOC}	r_{ProdL}	r_{ProdS}	$\propto \Omega$-1	k_T	F_{Surf}	F_{Bur}	Relative Error (%)	r^2
Sediment synthesis	—	—	—	—	No	0	—	0.130	—	1.0
Dunne et al. [2007] (initial)	1343	regional	—	—	No	0	0.339	0.212	92	0.34
F_{POC}	643	0.0602	0	0	No	0	0.362	0.130	75	0.34
$Prod_{Tot}$	643	0	0.00963	0.00963	No	0	0.389	0.134	54	0.57
$Prod_S$, $Prod_L$	643	0	0	0.01128	No	0	0.378	0.125	53	0.61
T, $Prod_S$, $Prod_L$	643	0	0	0.0167	No	−0.0189	0.374	0.121	48	0.62
Ω, F_{POC}	643	0.0231	0	0	Yes	0	0.410	0.158	64	0.48
Ω, $Prod_{Tot}$	643	0	0.00270	0.00270	Yes	0	0.368	0.130	77	0.55
Ω, $Prod_S$, $Prod_L$	643	0	0.00107	0.00295	Yes	0	0.363	0.125	79	0.55
Ω, T, $Prod_S$, $Prod_L$ (final)	643	0	0	0.01053	Yes	−0.0541	0.371	0.121	48	0.63

[a]Shown are the undersaturation-normalized depth scale for water column dissolution (z_{Diss}, m), proportionality to particulate organic carbon export (r_{FPOC}, dimensionless), proportionality to production by small phytoplankton (r_{ProdS}, dimensionless), Proportionality to Production by Large Phytoplankton (r_{ProdL}, dimensionless), whether or not to include a proportionality to the degree of supersaturation (Ω-1), and coefficient of temperature exponent (k_T, $^\circ C^{-1}$). Also shown are the global integral at water depths greater than 1000 m from 67°S–67°N for surface $CaCO_3$ production (F_{Surf}) and sediment $CaCO_3$ burial (F_{Bur}). Note that these integrals also necessarily exclude areas for which no GLODAP alkalinity and DIC were available for the calculations such as the Gulf of Mexico and inland seas as shown in Figures 4c and 4d. Also shown are the median relative error (median(model-obs)/obs*100; %) as in indication of the local uncertainty in F_{Bur} and the squared coefficients of determination (r^2) as an estimate of the fraction of variability in F_{Bur} captured by each configuration. In order to compare roughly normal distributions for the optimization and calculation of r^2, we used a $F^{1/3}$ transformation to remove the positive skew in the original flux distributions.

[22] Finally, adding a term for the slow respiration of organic matter within the sediments, $\phi_{Org} \cdot F_{Org}$, reduces preservation by reducing the saturation state of pore waters while compensating for the reduced importance of the rapidly respired fraction. As shown in Table 1, adding the slow respiration also enhances the importance of the exponents α and β and leads to the substantially smaller anomalies in Figure 3d. Overall, the five-parameter optimization brings the box model into excellent agreement with the full 1-D model ($r^2 = 0.98$).

2.4. Optimization of Surface Calcite Export Parameterization

[23] Surface calcite export (F_{Surf}) in our control case is based on satellite estimates of the export flux of organic carbon from *Dunne et al.* [2007] and regional estimates of the $Ca:C_{org}$ utilization ratio. As pointed out above, this approach skews the production of calcite to the ocean's subpolar areas and upwelling zones where the production of organic matter is high. Here, we examine several alternative ways of parameterizing the relationship between F_{Surf} and organic carbon production via combinations of particulate organic carbon export (F_{POC}), primary production by small ($Prod_S$) and large ($Prod_L$) phytoplankton, temperature (T) and supersaturation (Ω-1) following the general form of:

$$F_{Surf} = (r_{FPOC} \cdot F_{POC} + r_{ProdL} \cdot Prod_L + r_{ProdS} Prod_S) \cdot \exp(k_T \cdot T) \cdot (\Omega - 1) \quad (7)$$

The resulting parameter fits for the associated prefactors: r_{FPOC}, r_{ProdL}, r_{ProdS}, and k_T from (7) both with and without the assumed supersaturation functionality are summarized in Table 2. As indication of fitness of each optimization, we show the median relative error, and the corresponding 1/3 power transformed squared coefficient of determination (r^2) as an estimate of the fraction of the total variance in the observed estimates explained by each model algorithm. For reference on the underlying uncertainty in our target burial (Figure 1d), if we consider either of the two estimates of sediment accumulation rate that were geometrically averaged in this study as to get the target, we obtain a range for the median relative uncertainty of the other estimate of 46–62% as a rough target for the amount of agreement we should seek. The water column attenuation in our control case is retained. We show, first of all, that regional $Ca:C_{org}$ utilization ratios produce a better fit to the observed burial fluxes in Figure 1c in our control case: if the utilization ratio is set to the same value everywhere (third row in Table 2), the amount of observed flux variance explained by the predicted burial flux is reduced.

[24] F_{POC} is strongly influenced by the presence of large phytoplankton such as diatoms [e.g., *Tremblay et al.*, 1997], which tend to thrive in upwelling zones and subpolar areas. Because it distinguishes between the primary production by large phytoplankton (micro; >5 μm; $Prod_L$) and smaller pico (<2 μm) and nano (2–5 μm) phytoplankton ($Prod_S$), the estimate from *Dunne et al.* [2005, 2007] allows us to test the potential role of ecological diversity in driving calcite export. Indeed, when we switch from an F_{POC}-based algorithm to coupling F_{Surf} directly to $Prod_S$ and $Prod_L$, we find that the optimization selects a scenario in which F_{Surf} is associated exclusively with $Prod_S$. This had a strong, positive impact on the results, increasing the explained variance in the burial flux from 34% to 61% by removing much of the erroneous regional structure in the flux to the bottom seen in our control case (Figure 2b). Instead of the regional $Ca:C_{org}$ utilization ratios from the control case, a single scaling parameter is applied to the $Prod_S$ is used (fifth line of Table 2). This result is consistent with the ecological biodiversity control principles put forth by *Margalef* [1979] and others that the 'large' size class is primarily representative of diatoms and green alga, and that both they and their grazers - primarily crustacean zooplankton - are able to outcompete both autotrophic (coccolithophorids) and heterotrophic (foraminifera), leaving calcifiers to niches of lower productivity. These results are consistent with the *Schiebel* [2002] assessment of the relative importance of foraminifera on the global budget,

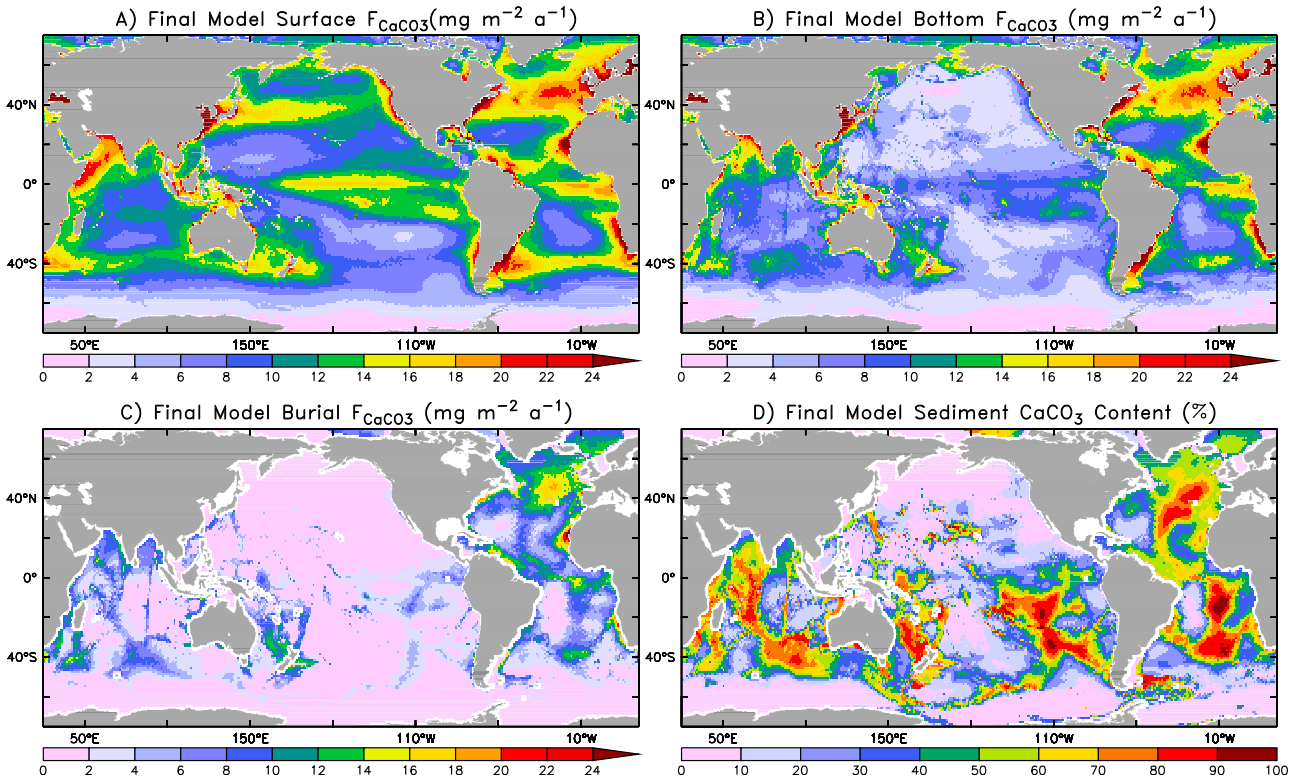

Figure 4. Maps of the final, optimized calcite cycle. (a) $CaCO_3$ production from the satellite synthesis using the algorithm based on Ω, temperature and small phytoplankton production in Table 2. (b) $CaCO_3$ flux to the ocean bottom using the production map in Figure 4a. (c) Optimized map of $CaCO_3$ burial flux based on the 5-parameter metamodel described in Table 1. (d) $CaCO_3$ content of modern sediment (%).

and noted lack of strong correlation between calcite flux and primary production.

[25] A negative temperature coefficient was also found to further increase the amount of variance explained to 62% (sixth line of Table 2). Coupling F_{Surf} to $Prod_S$ skews the F_{Surf} away from the margins and polar areas to the warmer low latitudes. The satellite-based primary production favors areas with warmer temperatures via the *Eppley* [1972] functionality of 0.063, so a small negative temperature coefficient in this case (−0.0189) serves to modestly diminish the temperature effect relative to primary production.

[26] Calcifying organisms have been shown to have calcification rates that are proportional to the level of supersaturation in the surface ocean [*Riebesell et al.*, 2000]. Hence, we have also evaluated a suite of F_{Surf} parameterizations that include a surface supersaturation factor, as has been done previously in three other recent global modeling studies [*Ridgwell and Hargreaves*, 2007; *Ridgwell et al.*, 2007a; *Gehlen et al.*, 2007]. The surface supersaturation factor improves the amount of variance explained, especially in the Atlantic, and yields an algorithm that can explain 63% of the burial flux (bottom line of Table 2). Because the supersaturation factor is also correlated with warmer temperatures (via the solubility of CO_2) a negative temperature coefficient (−0.0541) nearly as high as the original *Eppley* [1972] coefficient is needed to avoid double counting the impact of warmer temperatures on both saturation state and primary production. In this scenario, an optimal value for z_{Diss} was found to be 643 m, considerably shallower than our initial guess based on *Wong et al.* [1999].

3. Results

3.1. Regional and Global Summary

[27] Our final, optimal algorithm combines parameter values for burial efficiency via the last line in Table 1 into (6) and parameter values for surface calcite export (F_{Surf}) via the last line in Table 2 into (7) to yield F_{Surf} of 0.371 PgC a^{-1} (Figure 4a), a bottom flux (F_{Btm}) of 0.286 PgC a^{-1} (Figure 4b) and a burial flux (F_{Bur}) of 0.121 PgC a^{-1} for latitudes 67°S–67°N, water depths greater than 1000 m, and excluding inland seas for which no GLODAP DIC and alkalinity estimates were available. The fact that our F_{Surf} estimate is much lower than some estimates of total $CaCO_3$ export out of the euphotic zone summarized in *Berelson et al.* [2007] which vary between 0.5 and 4.7 PgC a^{-1}, is consistent with the present of other, more soluble forms of $CaCO_3$ that are not as easily exported through the water column and preserved on the sea and agree quite well with estimates of the upper-ocean export of 0.29 PgC a^{-1} in *Milliman* [1993] also based on deep sediment trap and sedimentation estimates and of the global burial flux of 0.13 PgC a^{-1} in *Milliman* [1993] and 0.10 PgC a^{-1} in *Catubig et al.* [1998]. We also have good agreement with the deep water sediment trap synthesis of *Honjo et al.* [2008]. See auxiliary material for details.

Table 3. Global Patterns in $CaCO_3$ Burial (F_{Bur}) From the Final Optimized Metamodel at Water Depths Greater Than 1000 m for the Ocean Divided Into Equal Areas With Respect to High/Low Bottom Water Saturation State (Ω) and High/Low $Caco_3$ Flux Out of the Surface Ocean (F_{Surf})

	High Ω[a]	Low Ω[a]
High F_{Surf}[b]	27% of area, 64% of burial, $F_{Bur}/F_{Surf} = 0.58$	23% of area, 11% of burial, $F_{Bur}/F_{Surf} = 0.12$
Low F_{Surf}[b]	23% of area, 22% burial, $F_{Bur}/F_{Surf} = 0.43$	27% of area, 4% of burial, $F_{Bur}/F_{Surf} = 0.06$

[a]Median value 0.844 used for cutoff.
[b]Median value 10.43 $gCaCO_3\ m^{-2}\ a^{-1}$ used for cutoff.

[28] By our estimate, three times as much calcite is produced in the upper ocean as is buried in ocean sediments at depths greater than 1000 m. This F_{Surf} estimate is slightly higher than our initial guess (third line in Table 3) based alkalinity:nitrate utilization gradients [*Sarmiento et al.*, 2002; *Dunne et al.*, 2007]. Expanded globally to all ocean areas however, our estimate grows to only 0.45 PgC a^{-1} compared to 0.52–0.58 PgC a^{-1} using the previous approach which was normalized to particle export.

[29] Figure 4c shows the spatial variation in the burial flux of the optimized model. Please note that the color scale has been stretched in Figure 4c in relation to the color scale for the observed fluxes in Figure 1c so that Figures 4a–4c all use the same scale. A more direct comparison is between our synthetic sediment composition (%$CaCO_3$) in Figure 4d and the observed sediment composition in Figure 1d. Overall, the model reproduces the main observed features, including the $CaCO_3$-rich areas in the Atlantic, along the mid-ocean ridges, and below the high productivity regions near 40°S.

[30] Skewing calcite export toward the open ocean areas of the tropics and subtropics dramatically improves the burial fluxes and sediment composition in the North Atlantic in relation to our control case in Figures 1c and 1d. Nevertheless, our model appears to underestimate burial in the North Pacific and Southern Ocean, and underestimate the burial in the southern Indian Ocean and along the equator in the Pacific. In the equatorial Pacific in particular, where glacial sedimentation rates are much higher than the present-day, this discrepancy may not be due to a model bias per se but an indication of relic calcite as sediment mixing processes and unusually abrupt changes in sedimentation rate allowing for a mixed glacial, early and late Holocene smearing [*Berelson et al.*, 1997]. Otherwise, our burial efficiencies are well in line with those estimated for the Ontong Java plateau (64–74% here; upper limit of 60–80% in *Hales and Emerson* [1996]), Ceara Rise above the saturation horizon (77–85% here; 80% in *Hales and Emerson* [1997a]), and Ceara Rise below the saturation horizon (58% here; 55% in *Hales and Emerson* [1997a]).

3.2. Quantification of Global Burial Controls

[31] Our modeling framework allows a means to quantify the roles for both respiration-driven dissolution, and supply driven preservation that both serve to decouple global calcite preservation from the saturation horizon. We find that the 21% of the seafloor below 1000 m in contact with super-saturated bottom water accounts for 54% of the burial flux. We find that organic respiration on the seafloor accounts for a majority (60%) of the dissolution below 1000 m, agreeing well with the main finding of *Archer* [1996], and that 88% of total sediment dissolution underlies undersaturated bottom waters, where the 'fast' respiration term contributes significantly.

[32] In Table 3, we divide up the ocean into quadrants in which the seafloor is represented as having either high or low overlying-water Ω, and receiving either high or low inputs from the surface ocean, respective to the global median values. The median calcite export out of the upper ocean in our analysis is F_{Surf}, is 10.43 $gCaCO_3\ m^{-2}\ a^{-1}$ and the median degree of calcite saturation at the seafloor is $\Omega = 0.844$. The four resulting quadrants have very nearly equal seafloor area (27, 23, 23, and 27% of the total ocean area), but very different calcite preservation characteristics. The high Ω, high F_{Surf} quadrant accounts for almost two thirds of the burial flux (64%) with the average burial flux in these areas equal to 58% of F_{Surf}. 49% of these locations are in the Atlantic and 24% are in the Indian. The high Ω, low F_{Surf} quadrant account for 22% of the overall burial. These are mostly shallow areas, along the crests of the mid-ocean ridges for example, where one might expect F_{Surf} to be mostly preserved. Nevertheless, only 43% of F_{Surf} is buried in these areas. The low Ω, high F_{Surf} quadrant account for an additional 11% of the burial. These areas include the equatorial and subpolar North Pacific. The low Ω, low F_{Surf} quadrant include the subtropical Pacific and abyssal Southern Ocean account for only 4% of burial with the average burial flux only 6% of F_{Surf}. While the role of Ω is clearly critical with two high Ω quadrants in Table 3 accounting for the most burial (86%), the role of supply is also important with the two high F_{Surf} quadrants in Table 3 accounting for nearly as much (75%).

4. Discussion

4.1. Mechanistic Controls on Calcite Preservation Efficiency

[33] One way to visually assess the importance of the surface export, interior dissolution, and sediment dissolution controls is to map the modeled burial distribution without these controls. Figure 5 shows the results of a set of sensitivity studies in which these controls are systematically re-introduced. In the first four scenarios, the saturation state of the water above the sediment varies by location while the surface and bottom calcite fluxes are held constant. The spatial distribution of the burial flux is shown in Figures 5a–5f. All scenarios are normalized by making the global flux of calcite to the sediments to yield the same globally integrated burial flux.

[34] For the illustration in Figure 5a, the flux of calcite to the sediments is assumed to be the same everywhere. Dissolution is governed by the observed saturation state of the water above the sediment alone; the organic respiration and

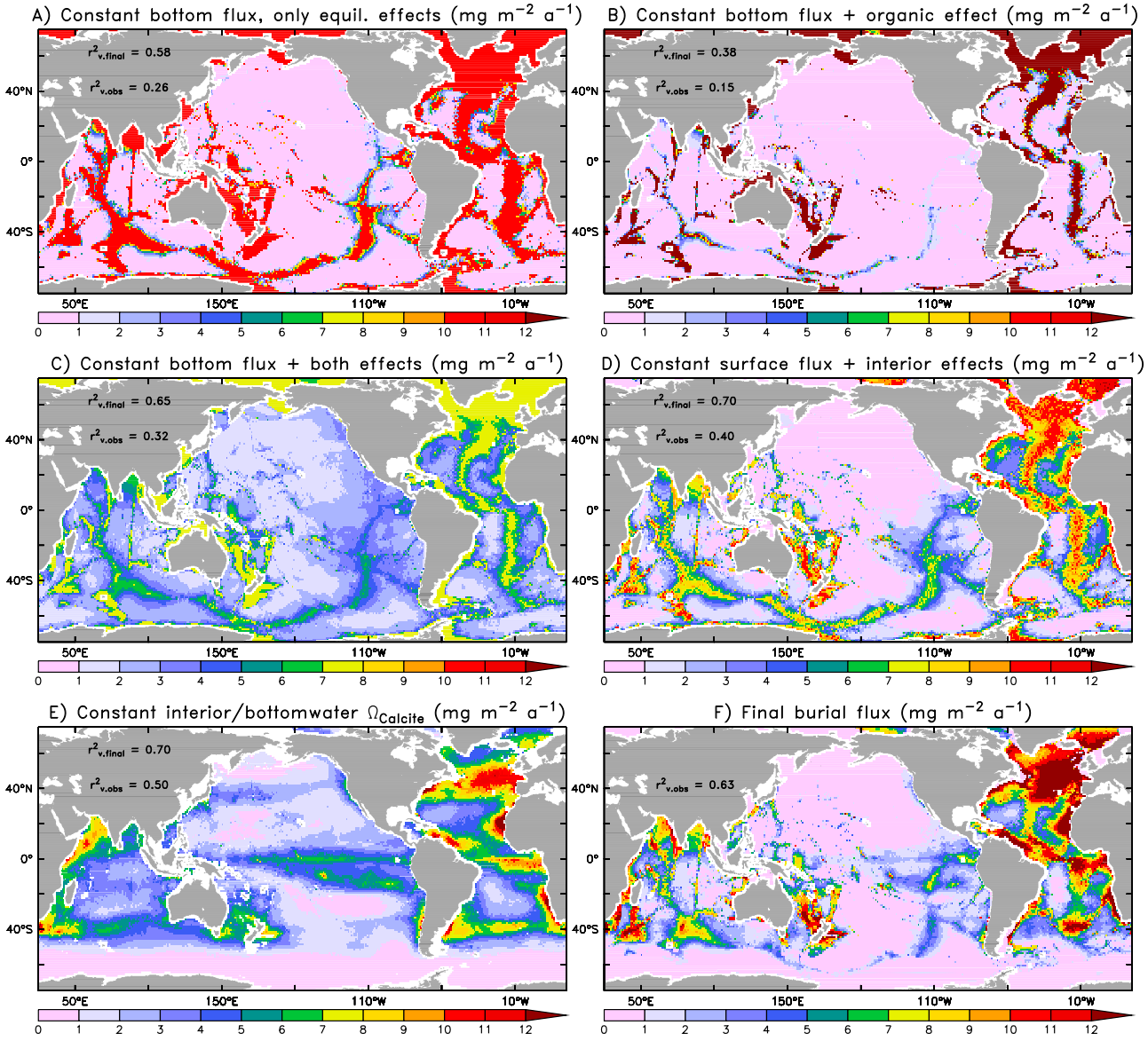

Figure 5. Sensitivity of $CaCO_3$ burial to assumptions governing regional variability in $CaCO_3$ flux and the role of kinetic and thermodynamic equilibrium factors in burial efficiency. (a) Assuming variable bottom water saturation state, but constant flux bottom sediments and ignoring the role of organic matter-enhanced dissolution through depression of pore water omega and dissolution-enhanced burial through elevation of pore water omega. (b) Like Figure 5a, except incorporating the organic matter enhanced dissolution effect. (c) Like Figure 5b, except including modulation of dissolution by incoming flux effect. (d) Assuming constant flux out of the ocean surface, but including regional variability in all interior effects. (e) Assuming regional variability in flux out of the surface ocean, but constant interior and bottom water omega. (f) The final, optimized burial flux including regional variability in all effects.

the flux-based dissolution effects have been ignored. The burial pattern in this case is what one would expect at the thermodynamic limit. The burial flux is large on ridge crests and on shallow banks and is zero everywhere else. The burial flux is also much greater than observed in the high latitudes. The effect of organic respiration is added for the illustration in Figure 5b. Organic respiration limits the areas of seafloor that can preserve calcite. As shown in Figure 5b, the water overlying the sediment has to be even more supersaturated in relation to the situation in Figure 5a for preservation to occur.

[35] For the illustration in Figure 5c, the flux-induced preservation term, $(F_{Lith} + F_{Btm})^{\beta}$, is added to the scenario in Figure 5b using a spatially uniform input of lithogenic material and calcite to examine the combined effects these of these factors in modulating dissolution. As dissolution due to undersaturated bottom waters and organic respiration is suppressed everywhere, some calcite is preserved everywhere, and intermediate burial efficiencies dominate.

[36] Ocean interior effects are illustrated in Figure 5d by setting F_{Surf} to a constant value and attenuating the flux of calcite to the sediment according to the saturation state and

bottom depth of the local water column. Water column dissolution, in this case, eliminates burial across much of the Pacific and in areas where the seafloor is especially deep and the interior is undersaturated. Preservation in the Atlantic is slightly improved. These results show that the lack of calcite burial in the deep Pacific owes much to water column dissolution as well as its undersaturated bottom waters.

[37] Thus far, bottom saturation state has been specified from observations. In Figure 5e, the opposite scenario is explored, wherein bottom and water column saturation states are held at a globally constant value while F_{Surf} is allowed to vary. The preservation in this case clearly reflects F_{Surf} in the optimized model (Figure 4a) modulated somewhat be water column depth (Figure 1a). Burial in polar regions is largely eliminated while burial in the subpolar Southern Ocean and the equatorial Pacific increases. This aspect of the vertical flux balance explains over two-thirds of the variability in the final model, and half of the variability in the observations.

[38] All the effects above are combined to produce the burial fluxes in Figure 5f, which can be directly compared with the observed burial flux in Figure 1c. The optimized model reproduces about 63% of the observed variability. The impact of the saturation state above the bottom is clearly less important in Figure 5f than it is in Figures 5a–5d, where F_{Surf} has no spatial variability. Meanwhile, the pattern of burial in the North Atlantic, tropical Atlantic, and the subpolar South Atlantic is clearly influenced by F_{Surf}, with most of the regional pattern in the calcite distribution seen in Figure 5f would remain even if the saturation state did not vary (Figure 5e). Burial in the sub-polar Indian and equatorial Pacific is similarly influenced.

[39] One somewhat counterintuitive result requiring discussion is that our box model requires a large exponent for the 1-Ω dissolution term in (6) even though the original functionality in the 1-D model is linear in 1-Ω. This is due to vertical gradients in sediment pore water that set up a nonlinear relationship between pore water and bottom water saturation states in the box model. This is expected from the results of *Hales* [2003] and *Hales and Emerson* [1997b] who showed nonlinear dissolution responses to bottom water undersaturation even for a linear kinetic representation of the dissolution rate, reflecting the increasing efficiency of near-interfacial dissolution as the under-saturation increases. Another interesting result is the need for a variable thickness of the actively dissolving sediment layer in order to account for decreased exposure time and enhanced preservation at high flux due to the kinetic limitations of diffusion to ventilate the pore water. Finally, both fast and slow organic matter degradation terms are required in order to account for the dissolution of calcite associated with the respiration of organic carbon.

4.2. Near-Term Implications for Calcification Under Global Warming and Acidification

[40] The functionality of calcite export based on supersaturation, small phytoplankton productivity and temperature developed here allows us to make a rough estimate of the deviation of present-day export from preindustrial times and the potential role of anticipated global warming and ocean acidification in the coming century based on the recent Intergovernmental Panel on Climate Change Fourth Assessment [*Meehl et al.*, 2007]. For this estimate, we utilized the sea surface temperature maps of the 2080–2100 average using the A1B scenario (pCO_2 = 683 ppm in 2090), the 1980–2000 historical average (pCO_2 = 353 μatm in 1990) and 1860–1880 historical average (pCO_2 = 286 μatm in 1860) taken from the GFDL CM2.1 climate model [*Delworth et al.*, 2006] to calculate temporal differences applied to the World Ocean Atlas temperature maps. This gave us globally averaged differences of −0.68 C for 1860 and 1.40 C for 2090 relative to modern conditions. To calculate supersaturation in 1860, we assumed that the average atmosphere-ocean ΔpCO_2 was zero. To calculate supersaturation in 2090, we made the assumption of constant atmosphere-ocean ΔpCO_2 over time over future increases (i.e., a constant lag in ocean uptake) and used the anticipated atmospheric change to calculate future surface ocean pCO_2. As a first approximation, we assumed that alkalinity and productivity were unchanged from the present-day. This resulted in calcite supersaturation averages of 4.4 for 1860, 3.7 for 1990 and 2.0 for 2090.

[41] Beginning with 0.45 PgC a^{-1} globally integrated calcite export for the 1990 case, we arrive at a 25% higher value of 0.57 PgC a^{-1} for 1860 and a 51% lower value of 0.22 PgC a^{-1} for 2090. More than three-quarters (77%) of the change from 1860 and 93% of the change in 2090 is due to changes in super-saturation rather than temperature. This point is highlighted when we choose an alternative formulation in Table 2 that includes only temperature and small phytoplankton production as predictors – an algorithm accounting for nearly as much of the variance in the sediment observations as the one including saturation state – in which the decrease in calcite productivity from 1990 to 2090 is only 4%. These relative estimates agree quite well with the model estimate by *Ridgwell et al.* [2007b] for a 13% decrease in calcite export between pre-industrial time and the present-day and a ∼50% decrease between preindustrial time and the year 2100. Estimates by *Heinze* [2004] and *Gehlen et al.* [2007] suggest a weaker calcite response. In any case, the true response is highly uncertain and in critical need for future study.

4.3. Inter-Basin Migration of Calcite Preservation Over Glacial Cycles

[42] The predominance of calcite-rich sediments in the Atlantic Ocean was significantly reduced at the Last Glacial Maximum (LGM) [*Biscaye et al.*, 1976]. At the same time, the zone of high-$CaCO_3$ sediments in the Pacific expanded as sediments on the flanks of the East Pacific rise became more $CaCO_3$-rich. In their analysis of equatorial Pacific sediment changes over time, *Farrell and Prell* [1989] showed that the 80% $CaCO_3$ contour deepened from 4200 m during the previous interglacial down to 4800 m at the onset of the LGM and then rose back up to 4200 m during the transition into the present interglacial. They argued that the changes in $\%CaCO_3$ are primarily driven by dissolution that reduces the $\%CaCO_3$ in this depth range from >80% during the LGM down to 50–60% during interglacials. The classical explanation for these glacial-interglacial changes is that the preservation of $CaCO_3$ seesaws back and forth between the Atlantic and Pacific in response to the position of the Atlantic lysocline. This idea is based on an assumption that the mean CO_3^{2-} for the deep ocean, the global production of $CaCO_3$, and the river input do not change significantly over time.

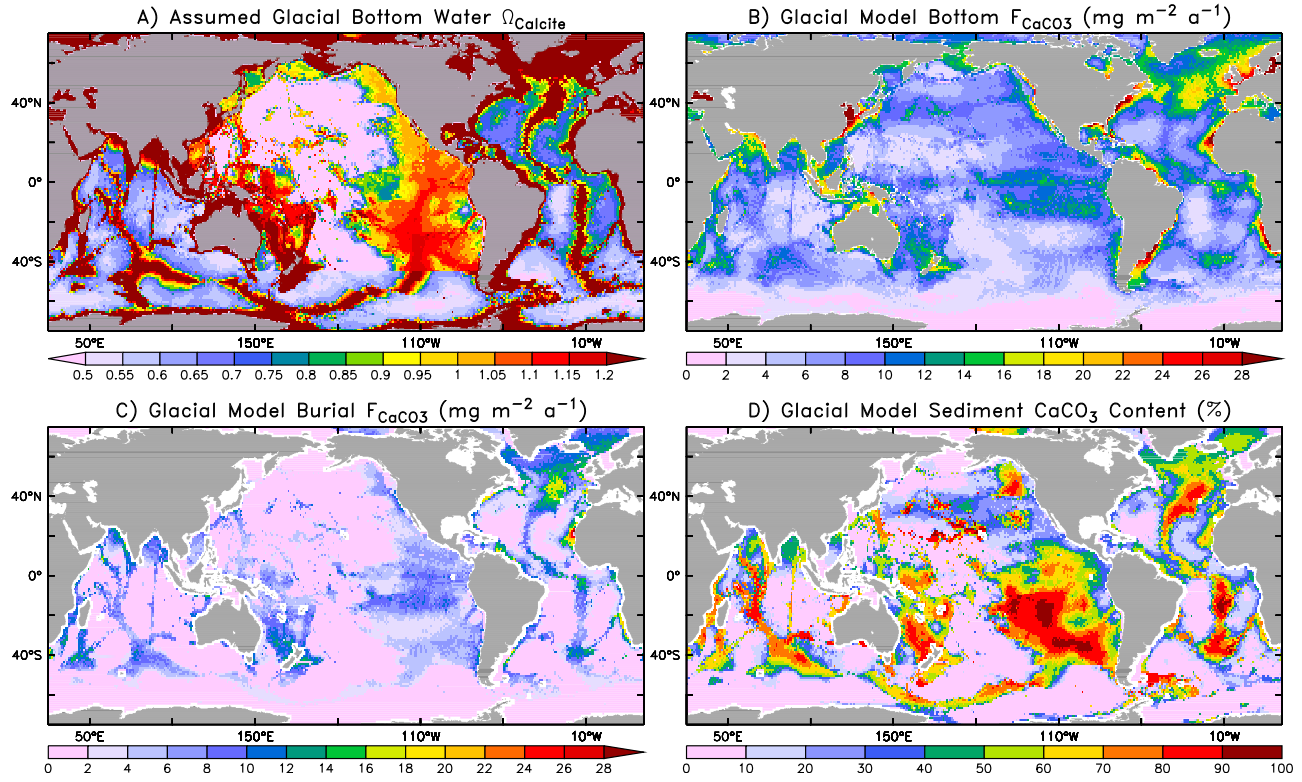

Figure 6. Maps of the inferred glacial calcite cycle from the CO_3^{2-} anomalies in *Broecker and Clark* [2001, Figure 7] with the deep Pacific tuned to match the global burial of the present-day. (a) Assumed glacial calcite saturation state of bottom water (Ω). (b) Inferred glacial $CaCO_3$ flux to the ocean bottom using the production map in Figure 4a. (c) Inferred glacial $CaCO_3$ burial flux. (d) Inferred $CaCO_3$ content of glacial sediment (%).

[43] One of the characteristics of the tropical Atlantic CO_3^{2-} profile today is relative homogeneity in the deep ocean with only a slight break at about 3500 m that marks the bottom of the saline core of NADW [*Broecker and Peng*, 1982]. Water below this depth is a mixture of northern and southern waters. The deep Pacific has similarly weak gradients. These patterns have been suggested to be dramatically different during the LGM when cold, high salinity [*Atkins et al.*, 2002], and low CO_3^{2-} bottom waters from the south invaded the deep Atlantic. *Broecker and Clark* [2001] and *Yu et al.* [2008] suggest that while CO_3^{2-} in the Atlantic during the LGM was about 27 μmol kg^{-1} higher than today, the bottom waters below were about 22 μmol kg^{-1} lower than today across a transition from 3000 m to 4000 m. These changes would have raised the saturation horizon in the Atlantic about 500 m (from 4500 m up to 4000 m), and produced a much sharper transition between supersaturated and undersaturated waters.

[44] CO_3^{2-} concentrations in the tropical Pacific today are about 30 μmol kg^{-1} below the Atlantic values. As such the CO_3^{2-} profile in the tropical Pacific crosses over the saturation horizon at approximately 3000 m. The *Farrell and Prell* [1989] results suggest that the lysocline was close to 4800 m at the LGM. *Broecker and Clark* [2001] argue that while tropical Pacific waters at 2300 m may have had CO_3^{2-} similar to today, tropical Pacific water at 4100–4400 m had CO_3^{2-} about 20 μmol kg^{-1} higher than today. Additionally, *Rickaby et al.* [2010] argue that average CO_3^{2-} in the deep ocean was roughly 20 μmol kg^{-1} higher during all the glacials of the last 800,000 years. As the long-term balance between calcite weathering and calcite burial appears to not have changed significantly between the LGM and the Holocene [*Catubig et al.*, 1998], we assume that these changes are not driven by calcite weathering.

[45] *Archer* [1991] pointed out that the $CaCO_3$-rich sediments observed at 4800 m in the equatorial Pacific during glacials require more local accumulation of $CaCO_3$, which could be due to either less dissolution or more export. We hypothesize that these changes were driven by the onset of abyssal stratification in the global ocean, which was shallower in the Atlantic, and deeper in the Pacific. Flooding of the abyssal Atlantic with dense, corrosive water from the south during the LGM caused lower Atlantic calcite burial, thus raising CO_3^{2-} in the deep ocean until burial in the east/central equatorial Pacific could make up the difference and establish a new equilibrium with the influx from weathering.

[46] In order to test this hypothesis, we ran our present-day model configuration of calcite flux out of the surface ocean (Figure 4a) with interior and bottom water CO_3^{2-} a continuous, empirical representation of the anomalies given in *Broecker and Clark* [2001], where CO_3^{2-} in the Atlantic, Indian and Southern Ocean were assumed to follow the Atlantic anomaly ($\Delta CO_3^{2-}{}_{Atl}$ = min(27,max(−22,(3640 − z) · 0.059)); umol kg^{-1}) and CO_3^{2-} in the abyssal Pacific north of 45°S was tuned to match the same global calcite burial as today by assuming the same strength of abyssal CO_3^{2-} stratification as in the

Atlantic and varying the depth of the Atlantic-type abyssal stratification ($\Delta CO_3^{2-}{}_{Pac}$ = min(21,28 · max (0,1 − exp((2300 − z)/1400))) − min(36,max(0,z − 4340) · 0.08)); umol kg^{-1}). The results of this retuning process are shown in Figure 6a, giving much lower inferred bottom water saturation states during the LGM below the mid-ocean ridges outside of the Pacific, and transitioning from higher-than-present to lower-than-present saturation states between 4000 m and 5000 m in the Pacific. The inferred bottom calcite fluxes are shown in Figure 6b. As expected due to the higher mid depth CO_3^{2-} in both oceans, bottom fluxes into areas with supersaturated bottom waters increase by 47%, while the flux to undersaturated bottom waters decreases by 21%. The inferred calcite burial fluxes are shown in Figure 6c. Total burial in supersaturated waters increases by 28% to go from 54% to 69% of the total.

[47] Inferred sediment calcite content (Figure 6d) show in general good agreement with the equatorial Pacific observations of *Farrell and Prell* [1989] and global data synthesis of *Catubig et al.* [1998] of enhanced tropical Pacific calcite content. As we saw when comparing our results for the present-day (Figure 4d) with observations from *Seiter et al.* [2004] (Figure 1d), our estimate for the North Pacific shows biases of enhanced burial relative to the observational estimate in *Catubig et al.* [1998]. Elsewhere, we find that the correspondence between saturation state (Figure 6a) and sediment calcite content (Figure 6d) during the LGM is far better than in the present ocean (Figures 1b and 4d, respectively) due to the enhanced deep stratification and associated gradient in CO_3^{2-}. Thus, this analysis suggests that the applicability of the lysocline as a representative of the saturation horizon may have been, somewhat ironically, more appropriate during the LGM than during the present-day. In this configuration, a combined reduction of 0.029 PgC a^{-1} calcite burial below 3500 m in the Atlantic, Indian, and Southern Oceans (24% of the interglacial total below 1000 m) is ultimately 83% balanced by enhanced burial in the Pacific and additionally augmented by enhanced burial along the mid-ocean ridges of the other oceans.

5. Conclusions

[48] We characterize geographically explicit and globally consistent representation of surface calcite export, interior dissolution and sediment dissolution by incorporating the role of pore water kinetic effects on calcite burial in the context of satellite, interior chemistry, and sediment burial observational constraints. Overall, we find that 48% of the burial of sediment calcite in the ocean occurs in sediments underlain by undersaturated bottom waters while 30% of sediment calcite dissolution occurs in sediments underlain by supersaturated bottom waters in the present-day ocean. We find that the most skillful predictor of surface calcite export is the primary production by small phytoplankton. This suggests that calcite export is ecologically more closely associated with the tightly recycling, small picoplankton and nanoplankton ecosystems than the blooming microplankton. We are unable to detect a strong role for saturation state on calcite export, but can only infer such an effect based on previous work if a corresponding strong compensating role of temperature is also assumed. Assuming both effects are at work, our sensitivity study of surface calcite production responses to projected centennial scale warming and acidification projects large decreases in surface calcite production over the 21st century. Alternatively assuming a weak temperature effect leads us to project a slight increase in surface calcite production over the 21st century, thus highlighting the continuing challenge in characterizing the global ocean acidification response. In the present-day ocean, we find the position of the lysocline to be strongly modulated by not only the saturation state of the bottom water but additionally the surface ocean ecology, pore water saturation, water depth and the supply of organic carbon to the sediments. During the last glacial maximum, the much stronger transition between calcite rich to calcite poor sediments in both oceans and the transition of burial from the deep Atlantic, Indian and Southern Oceans to the Pacific is consistent with the presence of intense abyssal stratification inferred from a variety of studies [e.g., *Broecker and Clark*, 2001; *Atkins et al.*, 2002] that drives a combined reduction of 0.029 PgC a^{-1} calcite burial below 3500 m in the Atlantic, Indian, and Southern Oceans and an overall alkalinity and CO_3^{2-} increase from interglacial into glacial periods until burial at mid-depth, largely in the Pacific, can compensate.

[49] **Acknowledgments.** We would like to thank NOAA's GFDL for supporting Toggweiler and Dunne, and NSF for supporting Hales. Eun Young Kwon, Anand Gnanadesikan, Jorge Sarmiento, Wolfgang Koeve, Eric Sundquist, Jess Adkins and an anonymous reviewer provided valuable criticism on the manuscript.

References

Archer, D. E. (1991), Equatorial Pacific calcite preservation cycles: Production or dissolution?, *Paleoceanography*, *6*, 561–571.

Archer, D. (1996), A data-driven model of the global calcite lysocline, *Global Biogeochem. Cycles*, *10*, 511–526.

Atkins, J. F., K. McIntyre, and D. P. Shrag (2002), The salinity, temperature, and $\delta^{18}O$ of the glacial deep ocean, *Science*, *298*, 1769–1773.

Berelson, W. M., et al. (1997), Biogenic budgets of particle rain, benthic remineralization and sediment accumulation in the equatorial Pacific, *Deep Sea Res., Part II*, *44*, 2251–2282.

Berelson, W. M., W. M. Balch, R. Najjar, R. A. Feely, C. Sabine, and K. Lee (2007), Relating estimates of $CaCO_3$ production, export, and dissolution in the water column to measurements of $CaCO_3$ rain into sediment traps and dissolution on the sea floor: A revised global budget, *Global Biogeochem. Cycles*, *21*, GB1024, doi:10.1029/2006GB002803.

Berger, W. H., C. G. Adelseck, and L. A. Mayer (1976), Distribution of carbonate in surface sediments of the Pacific Ocean, *J. Geophys. Res.*, *81*, 2617–2627.

Biscaye, P. E., V. Kolla, and K. K. Turekian (1976), Distribution of $CaCO_3$ in surface sediments of the Atlantic Ocean, *J. Geophys. Res.*, *81*, 2595–2603.

Broecker, W. S. (1971), Calcite accumulation rates and glacial to interglacial changes in ocean mixing, in *Late Cenozoic Glacial Ages*, edited by K. K. Turekian, pp. 239–265, Yale Univ. Press, New Haven, Conn.

Broecker, W. S., and E. Clark (2001), Glacial-to-Holocene redistribution of carbonate ion in the deep sea, *Science*, *294*, 2152–2155.

Broecker, W. S., and T.-H. Peng (1982), *Tracers in the Sea*, Lamont-Doherty Geol. Obs., Palisades, N.Y.

Catubig, N. R., D. E. Archer, R. Francois, P. deMenocal, W. Howard, and E.-F. Yu (1998), Global deep-sea burial rate of calcium carbonate during the last glacial maximum, *Paleoceanography*, *13*, 298–310.

Chung, S.-N., K. Lee, R. A. Feely, C. L. Sabine, F. J. Millero, R. Wanninkhof, J. L. Bullister, R. M. Key, and T.-H. Peng (2003), Calcium carbonate budget in the Atlantic Ocean based on water column inorganic chemistry, *Global Biogeochem. Cycles*, *17*(4), 1093, doi:10.1029/2002GB002001.

Conkright, M. E., H. E. Garcia, T. D. O'Brien, R. A. Locarnini, T. P. Boyer, C. Stephens, and J. I. Antonov (2002), *World Ocean Atlas 2001*, vol. 4 , *Nutrients*, *NOAA Atlas NESDIS*, vol. 52, NOAA, Silver Spring, Md.

Delworth, T. L., et al. (2006), GFDL's CM2 global coupled climate models. Part I: Formulation and simulation characteristics, *J. Clim.*, *19*, 643–674.

Dunne, J. P., R. A. Armstrong, A. Gnanadesikan, and J. L. Sarmiento (2005), Empirical and mechanistic models for particle export ratio, *Global Biogeochem. Cycles*, *18*, GB4026, doi:10.1029/2004GB002390.

Dunne, J. P., J. L. Sarmiento, and A. Gnanadesikan (2007), A synthesis of global particle export from the surface ocean and cycling through the ocean interior and on the seafloor, *Global Biogeochem. Cycles*, *20*, GB4006, doi:10.1029/2006GB002907.

Emerson, S., and M. L. Bender (1981), Carbon fluxes at the sediment-water interface of the deep sea: Calcium carbonate preservation, *J. Mar. Res.*, *39*, 139–162.

Eppley, R. W. (1972), Temperature and phytoplankton growth in the sea, *Fish. Bull.*, *70*, 1063–1085.

Farrell, J. W., and W. L. Prell (1989), Climatic change and $CaCO_3$ preservation: An 800,000-yr bathymetric reconstruction from the central equatorial Pacific Ocean, *Paleoceanography*, *4*, 447–466.

Feely, R. A., et al. (2002), In situ calcium carbonate dissolution in the Pacific Ocean, *Global Biogeochem. Cycles*, *16*(4), 1144, doi:10.1029/2002GB001866.

Feely, R. A., C. L. Sabine, K. Lee, W. Berelson, J. Kleypass, V. J. Fabry, and F. J. Millero (2004), Impact of anthropogenic CO_2 on the $CaCO_3$ system in the oceans, *Science*, *305*, 362–366.

Friis, K., R. G. Najjar, M. J. Follows, and S. Dutkiewicz (2006), Possible overestimation of shallow-depth calcium carbonate dissolution in the ocean, *Global Biogeochem. Cycles*, *20*, GB4019, doi:10.1029/2006GB002727.

Gehlen, M., R. Gangstøø, B. Schneider, L. Bopp, O. Aumont, and C. Ethe (2007), The fate of pelagic $CaCO_3$ production in a high CO_2 ocean: A model study, *Biogeosci. Discuss.*, *4*, 533–560.

Hales, B. (2003), Respiration, dissolution and the lysocline, *Paleoceanography*, *18*(4), 1099, doi:10.1029/2003PA000915.

Hales, B., and S. R. Emerson (1996), Calcite dissolution in sediments of the Ontong-Java Plateau: In situ measurements of porewater O_2 and pH, *Global Biogeochem. Cycles*, *10*, 527–541.

Hales, B., and S. R. Emerson (1997a), Calcite dissolution in sediments of the Ceara Rise: *In situ* measurements of porewater O_2, pH, and $CO_{2(aq)}$, *Geochim. Cosmochim. Acta*, *61*, 501–514.

Hales, B., and S. R. Emerson (1997b), Evidence in support of first-order dissolution kinetics for calcite in seawater, *Earth Planet. Sci. Lett.*, *48*, 317–327.

Hales, B., L. Burgess, and S. R. Emerson (1997), An absorbance-based fiber-optic sensor for $CO_{2(aq)}$ measurement in porewaters of sea floor sediments, *Mar. Chem.*, *59*, 51–62.

Heinze, C. (2004), Simulating oceanic $CaCO_3$ export production in the greenhouse, *Geophys. Res. Lett.*, *31*, L16308, doi:10.1029/2004GL020613.

Honjo, S., S. J. Manganini, R. A. Krishfield, and R. Francois (2008), Particulate organic carbon fluxes to the ocean interior and factors controlling the biological pump: A synthesis of global sediment trap programs since 1983, *Prog. Oceanogr.*, *76*, 217–285.

Jahnke, R. A. (1996), The global ocean flux of particulate organic carbon: Areal distribution and magnitude, *Global Biogeochem. Cycles*, *10*, 71–88.

Key, R. M., A. Kozyr, C. L. Sabine, K. Lee, R. Wanninkhof, J. L. Bullister, R. A. Feely, F. J. Millero, C. Mordy, and T.-H. Peng (2004), A global ocean carbon climatology: Results from Global Data Analysis Project (GLODAP), *Global Biogeochem. Cycles*, *18*, GB4031, doi:10.1029/2004GB002247.

Li, Y.-H., T. Takahashi, and W. S. Broecker (1969), Degree of saturation of $CaCO_3$ in the oceans, *J. Geophys. Res.*, *74*, 5507–5525.

Livingstone, D. A. (1963), *Chemical Composition of Rivers and Lakes*, *U. S. Geol. Surv. Prof. Pap.*, *440-G*, 64 pp.

Margalef, R. (1979), Life-forms of phytoplankton as survival alternatives in an unstable environment, *Oceanol. Acta*, *1*, 493–509.

Meehl, G. A., et al. (2007), Global climate projections, in *Climate Change 2007: The Scientific Basis: Contribution of Working Group I to the Fourth Assessment Report of the Intergovernmental Panel on Climate Change*, pp. 748–845, Cambridge Univ. Press, New York.

Milliman, J. D. (1993), Production and accumulation of calcium carbonate in the ocean: Budget of a nonsteady state, *Global Biogeochem. Cycles*, *7*, 927–957.

Milliman, J., P. J. Troy, W. Balch, A. K. Adams, Y.-H. Li, and F. T. MacKenzie (1999), Biologically mediated dissolution of calcium carbonate above the chemical lysocline?, *Deep Sea Res., Part I*, *46*, 1653–1669.

Morse, J., and F. T. Mackenzie (1990), *Geochemistry of Sedimentary Carbonates*, 707 pp., Elsevier, New York.

Najjar, R., and J. C. Orr (1998), Design of OCMIP-2 simulations of chlorofluorocarbons, the solubility pump and common biogeochemistry, internal OCMIP report, 25 pp., LSCE/CEA Saclay, Gif-sur-Yvette, France.

Nelder, J. A., and R. Mead (1965), A simplex method for function minimization, *Comput. J.*, *7*, 308–313.

Orr, J. C., et al. (2005), Anthropogenic ocean acidification over the twenty first century and its impact on calcifying organisms, *Nature*, *437*, 681–686.

Rickaby, R. E. M., H. Elderfield, N. Roberts, C.-D. Hillenbrand, and A. Mackensen (2010), Evidence for elevated alkalinity in the glacial Southern Ocean, *Paleoceanography*, *25*, PA1209, doi:10.1029/2009PA001762.

Ridgwell, A., and J. C. Hargreaves (2007), Regulation of atmospheric CO_2 by deep-sea sediments in an Earth system model, *Global Biogeochem. Cycles*, *21*, GB2008, doi:10.1029/2006GB002764.

Ridgwell, A., et al. (2007a), Marine geochemical data assimilation in an efficient Earth System Model of global biogeochemical cycling, *Biogeosciences*, *4*, 87–104.

Ridgwell, A., I. Zondervan, J. C. Hargreaves, J. Bijma, and T. M. Lenton (2007b), Assessing the potential long-term feedback of oceanic fossil fuel CO_2 uptake due to CO_2-calcification feedback, *Biogeosciences*, *4*, 481–492.

Riebesell, U., I. Zondervan, B. Rost, P. D. Tortell, R. E. Zeebe, and F. M. M. Morel (2000), Reduced calcification of marine plankton in response to increased atmospheric CO_2, *Nature*, *407*, 364–368.

Sarmiento, J. L., J. Dunne, A. Gnanadesikan, R. M. Key, K. Matsumoto, and R. Slater (2002), A new estimate of the $CaCO_3$ to organic carbon export ratio, *Global Biogeochem. Cycles*, *16*(4), 1107, doi:10.1029/2002GB001919.

Sayles, F. L. (1985), $CaCO_3$ solubility in marine sediments: Evidence for equilibrium and non-equilibrium behavior, *Geochim. Cosmochim. Acta*, *49*, 877–888.

Schiebel, R. (2002), Planktic foraminiferal sedimentation and the marine calcite budget, *Global Biogeochem. Cycles*, *16*(4), 1065, doi:10.1029/2001GB001459.

Seiter, K., C. Hensen, E. Schroter, and M. Zabel (2004), Organic carbon content in surface sediments—Defining regional provinces, *Deep Sea Res., Part I*, *51*, 2001–2026.

Tremblay, J. E., et al. (1997), Estimation of f-ratios in oceans based on phytoplankton size structure, *Limnol. Oceanogr.*, *42*, 595–601.

Turekian, K. K. (1964), The geochemistry of the Atlantic Ocean basin, *Trans N. Y. Acad. Sci.*, *26*, 312–330.

United Nations Educational, Scientific and Cultural Organization (1987), Thermodynamics of the carbon dioxide system in seawater: Report by the carbon dioxide sub-panel of the joint panel on oceanographic tables and standards, *U.N. Educ. Sci. Cult Organ. Tech. Pap. Mar. Sci. 51*, 55 pp., Paris.

Wong, C. S., F. A. Whitney, D. W. Crawford, K. Iseki, R. J. Matear, W. K. Johnson, J. S. Page, and D. Timothy (1999), Seasonal and interannual variability in particle fluxes of carbon, nitrogen and silicon from time series of sediment traps at Ocean Station P, 1982–1993: Relationship to changes in subarctic primary productivity, *Deep Sea Res., Part II*, *46*, 2735–2760.

Yu, J., H. Elderfield, and A. M. Piotrowski (2008), Seawater carbonate ion-$\delta^{13}C$ systematic and application to glacial-interglacial North Atlantic circulation, *Earth Planet. Sci. Lett.*, *271*, 209–220.